AIAA Journal
Vol. 42, No. 3, March 2004

Performance of High-Order-Accurate, Low-Diffusion Numerical Schemes for Compressible Flow

John A. Ekaterinaris*
Foundation for Research and Technology Hellas, 71110 Heraklion, Crete, Greece

High-order-accurate methods for the compressible flow equations in complex domains are evaluated. The first class of methods is appropriate for flows without discontinuities and uses high-order-accurate, centered space discretizations. The methods postprocess the computed solution with explicit spectral-type filters. The second class of methods uses centered schemes with characteristic-based filters and the artificial compression method, which makes it appropriate for discontinuous flows. The third class is the weighted essentially nonoscillatory finite difference schemes. Numerical solutions of model aeroacoustic problems and compressible flowfields are computed, and the accuracy of each method is evaluated.

I. Introduction

HIGH-ORDER-ACCURATE numerical solutions are required for direct and large eddy simulations (LES) of compressible flows where the diffusion of the numerical solution must be kept at a very low level to preserve small-scale turbulent fluctuations. Aeroacoustics is another area where accurate convection of small-scale disturbances plays a crucial role. Total variation diminishing (TVD), shock-capturing schemes are not usually optimal for LES of turbulent flow or computation of aeroacoustic disturbances. In recent years, there have been numerous efforts in optimizing these schemes[1] to make possible LES computations of shock/turbulence interaction and aeroacoustic noise sources, where small scales can be seriously diffused by the numerical dissipation, which is necessary to resolve shock waves.

Numerical solutions of flows over wings at high incidence and over helicopter rotors require high resolution, often achieved by the use of a large number of grid points, to preserve tip vortices, vortical wakes, and detached shear layers that have a significant influence on loading. For these problems, as an alternative to high grid density, methods that are high-order accurate in space may be used. High-order-accurate numerical solutions with nondissipative centered schemes have an advantage over shock-capturing schemes for aeroacoustics and isotropic problems, such as vortex convection. However, centered schemes discretizations of nonlinear problems require some form of numerical smoothing to eliminate high-frequency oscillations arising from nonlinear instabilities. Yee et al.[2] have developed characteristic-based filters. Gaitonde and Visbal[3] have used spectral-type filters, which have improved properties compared to similar filters proposed by Lele.[4] On the other hand, essentially nonoscillatory (ENO) schemes[5,6] avoid oscillations by choosing among available stencils around the discontinuity. Recently, weighted essentially nonoscillatory (WENO) schemes[7] have been developed as a follow-up of ENO schemes to cure the order dependency of ENO related to the free stencil adaptation in smooth regions. WENO schemes use a convex combination of the ENO stencils. They assign almost zero weight to the stencil that includes the discontinuity and at the same time yield a higher order of accuracy for the same stencil size compared to ENO schemes.

The objectives of this work are to evaluate the accuracy of existing high-order-accurate finite difference methods and apply them for the computation of flows in complex domains, where the use of a curvilinear stretched grid is necessary. Three different high-order-accurate, low-diffusion finite difference methods are evaluated. The first two methods use centered compact space differentiation of the convective fluxes. The first method[8] is appropriate only for computations of flows without discontinuities, such as low-Mach-number subsonic flows and aeroacoustic problems. It has been developed and tested by Gaitonde and Visbal[3] and Visbal and Gaitonde.[8,9] This method was recently used for LES of compressible flows.[10] It performs high-order-accurate, compact space discretization of the convective fluxes[4] and postprocesses the computed solution with a spectral-type low-pass filter[3] to eliminate nonlinear instability, aliasing errors, and spurious modes of the solution occurring from the application of boundary conditions. The second method[2] can be used for high-resolution computations of flows with discontinuities. It also uses centered fourth- or sixth-order-accurate discretization of the convective fluxes and characteristic-based filters[2] combined with the artificial compression sensor of Harten.[11] This method is similar to the fourth-order-accurate scheme of Ref. 12, which uses artificial numerical smoothing. It has been demonstrated[1,2] that the characteristic-based filters can significantly reduce numerical diffusion. The third method is the curvilinear coordinates form of high-order-accurate WENO schemes.[7] In addition, the compact WENO scheme recently proposed by Pirozzoli[13] is also used.

The ability of all high-order accurate stencils to perform long time integration is evaluated first. Computations of aeroacoustic disturbances with the numerical solution of the full nonlinear Euler equations are carried out next. Finally, the shock-capturing capability of centered schemes with characteristic filters and WENO schemes of different order is evaluated.

II. Governing Equations

The strong conservation law form of the full compressible Navier–Stokes equations in curvilinear coordinates is

$$\frac{\partial}{\partial t}\left(\frac{\boldsymbol{Q}}{J}\right)+\frac{\partial \boldsymbol{E}}{\partial \xi}+\frac{\partial \boldsymbol{F}}{\partial \eta}+\frac{\partial \boldsymbol{G}}{\partial \zeta}=\frac{1}{Re}\left[\frac{\partial \boldsymbol{E}_v}{\partial \xi}+\frac{\partial \boldsymbol{F}_v}{\partial \eta}+\frac{\partial \boldsymbol{G}_v}{\partial \zeta}\right] \qquad (1)$$

In Eq. (1), $\boldsymbol{Q}=\{\rho, \rho u, \rho v, \rho w, \rho E\}^T$ denotes the solution vector, $J=\partial(x, y, z)/\partial(\xi, \eta, \zeta)$ is the Jacobian of the transformation, and $\boldsymbol{E}, \boldsymbol{F}$, and $\boldsymbol{G}$ and $\boldsymbol{E}_v, \boldsymbol{F}_v$, and $\boldsymbol{G}_v$ are the inviscid and viscous flux vectors, respectively.

III. Numerical Method

Space discretization of the governing equations (1) is performed with high-order-accurate finite difference schemes. Time marching

---

Received 31 May 2003; presented as Paper 2003-3539 at the 16th Computational Fluid Dynamics Conference, Orlando, FL, 23 June 2003; revision received 3 October 2003; accepted for publication 6 October 2003.

*Research Director, Numerical Analysis and Scientific Computing Group, Institute of Applied and Computational Mathematics, P.O. Box 1527; ekaterin@iacm.forth.gr. Associate Fellow AIAA.

is performed by both implicit and explicit methods. Time and space discretization methods are summarized next.

A. Temporal Schemes

The third-order-accurate Runge–Kutta (RK3) method (see Refs. 6, 14, and 15) is used for explicit time marching. Furthermore, the factored, implicit, second-order accurate in space and time Beam–Warming algorithm[16] (BW-22) that overcomes stability limitations of explicit methods can be used. The BW-22 algorithm augmented with Newton-like subiterations is

$$\left[I + (\theta \quad \Delta t)\delta_\xi \left(\frac{\partial \boldsymbol{E}}{\partial \boldsymbol{Q}}\right)^p\right] \times \left[I + (\theta \quad \Delta t)\delta_\eta \left(\frac{\partial \boldsymbol{F}}{\partial \boldsymbol{Q}}\right)^p\right]$$

$$\times \left[I + (\theta \quad \Delta t)\delta_\zeta \left(\frac{\partial \boldsymbol{G}}{\partial \boldsymbol{Q}}\right)^p\right] \Delta \boldsymbol{Q}^p$$

$$= -\theta \Delta t \left[\frac{(1+\theta)\boldsymbol{Q}^p - (1+2\theta)\boldsymbol{Q}^n + \theta \boldsymbol{Q}^{n-1}}{\Delta t}\right.$$

$$\left. + \left(\delta_\xi \boldsymbol{E}^p + \delta_\eta \boldsymbol{F}^p + \delta_\zeta \boldsymbol{G}^p\right)\right] = \mathrm{RHS}^p \tag{2}$$

where $\theta = 1/(1+\vartheta)$, RHS is the right-hand side, and $\Delta \boldsymbol{Q}^p = \boldsymbol{Q}^{p+1} - \boldsymbol{Q}^p$. The implicit, iterative scheme of Eq. (2) yields first- ($\vartheta = 0$) or second-order ($\vartheta = \frac{1}{2}$) accuracy in time. For one subiteration, $p = 1$ and $\boldsymbol{Q}^p = \boldsymbol{Q}^n$, and, as $p \to \infty$, linearization and factorization errors are eliminated and $\boldsymbol{Q}^p \to \boldsymbol{Q}^{n+1}$.

The spatial derivatives in Eq. (2) are computed with second-order-accurate finite differences to retain the block tridiagonal structure of the implicit operators. The original implicit scheme of Eq. (2) (BW-22) algorithm was modified in Ref. 17 to obtain higher-order spatial accuracy. It was shown[17] that use of compact fourth-order-accurate formulas retains the block tridiagonal structure of the implicit operators and yields fourth-order spatial accuracy. The resulting (BW-24) algorithm requires only a negligible increase in computing cost.

B. High-Order Centered Schemes

A five-point wide stencil, finite difference discretization of any spatial derivative of a scalar pointwise discrete quantity f in Eq. (1), such as metric terms or flow variables, is obtained in the computational domain by

$$Bf'_{j+2} + Af'_{j-1} + f'_j + Af'_{j+1} + Bf'_{j+2} = a[(f_{j+1} - f_{j-1})/2]$$

$$+ b[(f_{j+2} - f_{j-2})/4] + c[(f_{j+3} - f_{j-3})/4] \tag{3}$$

where A, B, a, b, and c determine the spatial accuracy of the discretization. Different values of the coefficients in the formula of Eq. (3) yield schemes of different accuracy, ranging from the 4th-order explicit method to the compact 10th-order-accurate scheme. The values of the coefficients in Eq. (3) for schemes of different orders of accuracy can be found in Refs. 4 and 9. Stable, accurate formulas for the boundary points can be found in Ref. 18. Numerical solutions of nonlinear hyperbolic equations with central-difference methods develop spurious modes arising from unresolvable scales and inaccuracies in the application of boundary conditions. The development and application of spectral-type filters that can be used to stabilize numerical solutions performed with central-difference methods for flows without discontinuities are given in Ref. 3.

C. Characteristic-Based Filters

The characteristic filter[2] can be used in combination with central-difference high-order-accurate schemes for both smooth flows and flows with discontinuities. This filter is applied on the solution vector, $\bar{\boldsymbol{Q}}^{n+1}$, either at the end of a Runge–Kutta step or at the end of a full implicit sweep after the completion of the pth subiteration with Eq. (2). After filtering, the solution $\boldsymbol{Q}^{n+1}$at the new time level is defined as

$$\boldsymbol{Q}^{n+1} = \bar{\boldsymbol{Q}}^{n+1} + \Delta t L_f(\boldsymbol{E}^*, \boldsymbol{F}^*, \boldsymbol{G}^*)_{i,j,k} \tag{4}$$

The filter operator $L_f(\boldsymbol{E}^*, \boldsymbol{F}^*, \boldsymbol{G}^*)_{i,j,k}$ is applied for each flux on a dimension-to-dimension basis. For example, the filter operator for the flux F is

$$L_f(\boldsymbol{F}^*)_{i,j,k} = (1/\Delta\eta)\left[\tilde{\boldsymbol{F}}^*_{i,j+\frac{1}{2},k} - \tilde{\boldsymbol{F}}^*_{i,j-\frac{1}{2},k}\right] \tag{5}$$

The filter dissipative numerical fluxes $\tilde{\boldsymbol{F}}^*_{i,j+1/2,k}$ for the operator of Eq. (5) are evaluated at $\bar{\boldsymbol{Q}}^{n+1}$. They have the form

$$\tilde{\boldsymbol{F}}^*_{i,j+\frac{1}{2},k} = \tfrac{1}{2} R_{j+\frac{1}{2}} \Phi^*_{j+\frac{1}{2}} \tag{6}$$

where $R_{j+1/2}$ is the right eigenvector matrix of the flux Jacobian $B = \partial \boldsymbol{F}/\partial \boldsymbol{Q}$. The elements $\phi^{l^*}_{j+1/2}$ of $\Phi^*_{j+1/2}$ are given by

$$\phi^{l^*}_{j+\frac{1}{2}} = \kappa \theta^l_{j+\frac{1}{2}} \phi^l_{j+\frac{1}{2}} \tag{7}$$

where $\phi^l_{j+1/2}$ are the nonlinear dissipation portions of a TVD, ENO, or WENO scheme.[2,19] The function $\kappa\theta^l_{j+1/2}$ is the key mechanism to achieve high accuracy for the fine-scale structures and smooth regions of the flow, as well as stability and shock capturing. The parameter κ is problem dependent[2] and ranges as $0.03 < \kappa < 2$. The function $\theta^l_{j+1/2}$ is the Harten switch[11] given by

$$\theta^l_{j+\frac{1}{2}} = \max\left(\hat{\theta}^l_{j-m+1}, \ldots, \hat{\theta}^l_{j+m}\right), \qquad \hat{\theta}^l_j = \left|\frac{\left|\alpha^l_{j+\frac{1}{2}}\right| - \left|\alpha^l_{j-\frac{1}{2}}\right|}{\left|\alpha^l_{j+\frac{1}{2}}\right| + \left|\alpha^l_{j-\frac{1}{2}}\right|}\right| \tag{8}$$

where $\alpha^l_{j-1/2}$ are the elements of the left eigenvector matrix $R^{-1}_{j+1/2}$ of the flux Jacobian $B = \partial F/\partial q$.

D. WENO Schemes

The basic problem of the ENO finite difference formulation is the conservative approximation of the derivative u' of a function $u(x)$ starting from the pointwise values of the function (finite difference approach) given on a set of grid points $u_i = u(x_i)$, $i = 1, 2, \ldots, N$, with uniform grid spacing h. Note that the uniform grid assumption is essential for the development of finite difference ENO and WENO schemes. The approximation of the derivative $u'(x_i)$ to kth-order accuracy is achieved when a numerical flux function $\tilde{u}_{i+1/2}$ at the intermediate nodes $i + \frac{1}{2}$ and $i - \frac{1}{2}$ can be found so that $(1/h)(\tilde{u}_{i+1/2} - \tilde{u}_{i-1/2}) = u'(x_i) + \mathcal{O}(h^k)$, $i = 1, 2, \ldots, N$. It was shown[5,20] that the solution to this problem is equivalent to the interpolation problem where the reconstruction of the function $u(x)$ at the intermediate nodes $\tilde{u}_{i+1/2}$ is evaluated starting from its cell-averaged values:

$$\bar{u}_i = \int_{x_{i-\frac{1}{2}}}^{x_{i+\frac{1}{2}}} u(x)\,\mathrm{d}x$$

The approximation of the derivative is kth-order accurate when the condition $\tilde{u}_{i+1/2} = u_{i+1/2} + \mathcal{O}(h^k)$ is satisfied. For a k point stencil $x_{i-r}, \ldots, x_{i+s}$, where $r + s = k - 1$, the numerical flux $\tilde{u}_{i+1/2}$ is expressed as

$$\tilde{u}_{i+\frac{1}{2}} = \sum_{j=0}^{k-1} c_{rj} u_{i-r+j} \tag{9}$$

where the coefficients c_{rj} (see Ref. 20) yield different stencils for kth-order-accurate approximations with Eq. (9). Given the k stencils for the approximations of the numerical flux $\tilde{u}_{i+1/2}$, ENO piecewise polynomial reconstruction of degree at most $k - 1$ can be obtained. This is achieved by adaptively selecting the appropriate stencils based on the absolute values of divided differences. The resulting ENO reconstruction is uniformly high-order accurate up to the discontinuity, and the accuracy condition is satisfied for any cell in the smooth flow regions.

The reconstruction process has the following drawbacks. The free adaptation of the stencil with the ENO reconstruction process is not necessary in smooth flow regions. The appropriate stencil is selected among k candidate stencils that cover $2k-1$ cells, and the stencil choosing procedure is time consuming. The most recent attempt to improve on ENO is the WENO scheme that uses a convex combination of all k potential stencils to obtain $(2k-1)$th-order accuracy in smooth regions. WENO reconstruction with a convex combination of all values of the numerical flux $\tilde{u}^{(r)}_{i+1/2}$ of Eq. (9) is obtained with the following approximation:

$$\tilde{u}_{i+\frac{1}{2}} = \sum_{r=0}^{k-1} \omega_r \tilde{u}^{(r)}_{i+\frac{1}{2}}, \qquad \omega_r \geq 0, \qquad \sum_{r=0}^{k-1} \omega_r = 1 \tag{10}$$

The weights of Eq. (10) are computed as

$$\omega_r = \alpha^r / (\alpha^1 + \cdots + \alpha^{k-1}), \qquad r = 0, \ldots, k-1$$

$$\alpha^r = d_r \Big/ (\varepsilon + \beta_r)^2 \tag{11}$$

where ε is a small parameter to avoid division by zero ($\varepsilon = 10^{-6}$) and B_r are the so-called smoothness indicators.

Smoothness indicators and WENO weights are tabulated in Refs. 6, 20, and 21. High-order WENO stencils[21] for $r = 4$, 5, and 6 that yield $(k = 2r-1)$th-order accuracy are fifth-order accurate for $r = 3$:

$$\tilde{f}_{i+\frac{1}{2}} = (1/30) f_{i-2} - (13/60) f_{i-1} + (47/30) f_i + (9/20) f_{i+1} - (1/20) f_{i+2} \tag{12}$$

seventh-order accurate for $r = 4$:

$$\begin{aligned}\tilde{f}_{i+\frac{1}{2}} = {} & -(1/140) f_{i-3} + (5/84) f_{i-2} - (101/420) f_{i-1} \\ & + (319/420) f_i + (107/210) f_{i+1} + (19/210) f_{i+2} \\ & + (1/105) f_{i+3}\end{aligned} \tag{13}$$

and ninth-order accurate for $r = 5$:

$$\begin{aligned}\tilde{f}_{i+\frac{1}{2}} = {} & (1/630) f_{i-4} - (41/2520) f_{i-3} + (199/2520) f_{i-2} \\ & - (641/2520) f_{i-1} + (1789/2520) f_i + (275/504) f_{i+1} \\ & - (61/504) f_{i+2} + (11/504) f_{i+3} - (1/504) f_{i+4}\end{aligned} \tag{14}$$

Furthermore, the following compact WENO scheme developed by Pirozzoli[13] may be used for the evaluation of the numerical flux with fifth-order accuracy:

$$9\tilde{f}_{i-\frac{1}{2}} + 18\tilde{f}_{i+\frac{1}{2}} + 3\tilde{f}_{i+\frac{3}{2}} = f_{i-1} + 19 f_i + 10 f_{i+1} \tag{15}$$

The compact WENO scheme of Eq. (15) has improved resolution in wave space[13] compared to equivalent or higher-order explicit WENO stencils of Eqs. (12) and (13).

The Lax–Friedrichs flux or the Roe flux can be used as building blocks with the WENO schemes of Eqs. (12–15). Evaluation of the Lax–Friedrichs flux is less computationally intensive, and, for high-order WENO schemes, no significant differences are observed from the results obtained with Roe's flux. For the evaluation of the conservative kth-order approximation of the flux derivative $\partial \boldsymbol{F}_j / \partial \eta = (\tilde{\boldsymbol{F}}_{j+1/2} - \tilde{\boldsymbol{F}}_{j-1/2}) / \Delta\eta + O(\Delta\eta^k)$, the numerical flux $\tilde{\boldsymbol{F}}_{j+1/2}$ with WENO schemes of different order of accuracy $O(2r-1)$ can expressed as

$$\tilde{\boldsymbol{F}}_{j-\frac{1}{2}} = \sum_{m=j-r+2}^{j+r-1} c_m \boldsymbol{F}_m + R^{-1}_{j+\frac{1}{2}} \varphi_N(a_0, a_1, \ldots, a_{2r-1}) \tag{16}$$

where the first part is a central interpolation of the physical flux $\boldsymbol{F}_j$ combined with the WENO part $\varphi_N(a_0, a_1, \ldots, a_{2r-1})$ that includes the smoothness measures of Eqs. (10) and (11) and the building block Lax–Friedrichs flux $\boldsymbol{F} = \boldsymbol{F}^+ + \boldsymbol{F}^-$ and $\boldsymbol{F}^\pm = \boldsymbol{F} + \alpha \boldsymbol{Q}$ where $\alpha = \lambda$ and λ is the maximum eigenvalue of the flux Jacobian. To have continuous higher derivatives of the split fluxes, select $\alpha = \sqrt{(\varepsilon^2 + \lambda^2)}$ and $\varepsilon = 0.05$.

Boundary conditions for WENO schemes are difficult to formulate. One possibility is to preserve formal order of accuracy and switch from WENO to standard extrapolation on the boundaries. Another possibility is to reduce the order of accuracy on the boundary with lower order stencils. The ghost approach that makes the overall scheme more stable and does not require branching for boundary treatment is used in this work.

IV. Results

The resolving ability and the performance for long time integration of the numerical schemes presented in the preceding section are evaluated first for simple linear problems. The performance of centered and WENO schemes for aeroacoustics by the use of the full Euler equations is considered next. Finally, centered schemes with characteristic-based filters are compared with WENO schemes for problems with strong shocks in curvilinear coordinates. The computed solutions are compared with available exact solutions.

A. Performance for Linear Convection

Long time integration is important in many practical applications, such as aeroacoustics, LES, and helicopter rotor calculations where the tip vortex and the rotor wake need to propagate for long distances. Therefore, the ability of symmetric, centered compact, and noncompact schemes, as well as several WENO high-order-accurate stencils is evaluated first for wave convection. Sufficiently accurate convection of simple Gaussian pulses, $u(x, t=0) = e^{-ax^2}$, with 12 points per waveform (not shown here) was achieved even with explicit fourth-order accurate in space methods.

Further accuracy tests are shown for linear wave convection by the one-dimensional wave equation $u_t + c u_x = 0$. Numerical solutions with unit wave speed $c = 1$ are obtained for long propagation times. Time marching is performed with the RK3 method.[6,14] A time step of $\Delta t = 0.1$, which is below the stability limit of the method, is used for all tests to keep time integration errors at low level.

The first test is propagation of a high-frequency sinusoidal wave $u_0(x) = \sin(\pi x/6)$. Convection of the sinusoidal wave is obtained with $\Delta x = 0.1$ (12 points per wavelength) and periodic boundary conditions. The mean square error obtained from explicit space discretizations with the symmetric fourth- and sixth-order-accurate schemes and with WENO schemes of fifth- and seventh-order accuracy [Eqs. (12) and (13)] is shown in Table 1. It appears that only the schemes with formal accuracy of more than five are capable of obtaining a sufficiently accurate solution for long time integration.

Further evaluation of high-order-accurate symmetric explicit and compact schemes and WENO stencils to perform linear wave convection is carried out with the following modulated wave $u_o(x) = \cos(a|x|)e^{-b|x|}$ with $a = 3/4$ and $b = 1/10$ as initial condition. For explicit schemes, time integration is performed until $T = 200$. For compact schemes, which have increased resolving ability, time integration is performed until the final time $T = 500$. A comparison of the solutions computed using explicit high-order symmetric schemes and WENO stencils with the exact result is shown in Fig. 1. Note that at least sixth-order accuracy is needed for long time propagation. The mean square error of the solutions computed with different schemes is shown in Tables 2 and 3. It appears that the ninth-order-accurate WENO stencil provides a uniformly high order of accuracy for smooth initial data.

Table 1 L_2 error at $T = 200$ for the convection of $\sin(\pi x/6)$ with explicit schemes

Explicit schemes	L_2 error
4th-order centered	$0.2E00$
6th-order centered	$0.11E{-}2$
5th-order WENO	$0.12E{-}1$
7th-order WENO	$0.14E{-}3$

Table 2 L_2 error at $T=200$ for the convection of $\cos(a|x|)e^{-b|x|}$ with explicit schemes

Scheme	L_2
6th-order centered	$0.4E$–3
5th-order WENO	$0.1E$–2
7th-order WENO	$0.7E$–4
9th-order WENO	$0.7E$–2

Table 3 L_2 error at $T=500$ for the convection of $\cos(a|x|)e^{-b|x|}$ with compact schemes

Compact scheme	L_2 error
5th-order WENO	$0.19E$–3
6th-order centered	$0.57E$–4
8th-order centered	$0.92E$–5
10th-order centered	$0.53E$–5

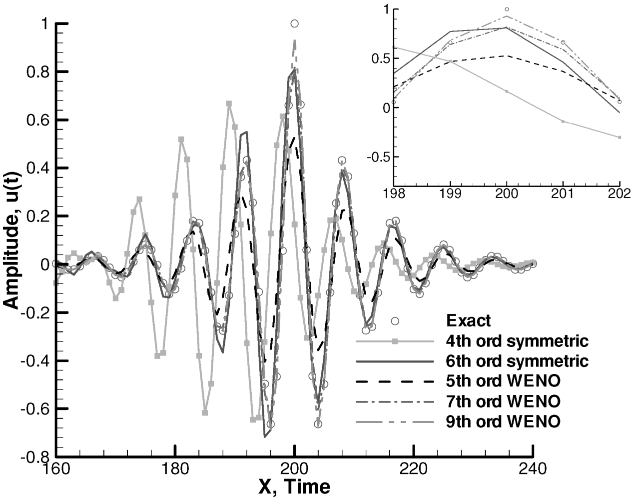

Fig. 1 Comparison of the exact solution $u_o(x)=\cos(a|x|)e^{-b|x|}$ at $T=200$ with results computed with explicit schemes.

The mean square error for long time integration, $T=500$, of high-order compact schemes (Table 3) also remains at low levels. Note that compact schemes with formal order of accuracy more that four perform adequately. The high-order-accurate compact schemes appear to be particularly suitable for linear aeroacoustic problems.

The computing time the explicit schemes is proportional to the width of the stencil. The computing cost of the 8th- and 10th-order compact schemes that require pentadiagonal matrix inversion is the highest and almost double compared to the time required by the explicit schemes. However, the use of very high-order centered methods may be required for wave convection over long time periods.

B. Performance for Aeroacoustics

Symmetric schemes with spectral-type filtering and characteristic-based filters, as well as WENO schemes of different orders of accuracy, are used to compute spread and reflection of a pressure disturbance. The full nonlinear Euler equations are used for this test. At the far-field boundaries of the domain, a radiation boundary condition was used. On the solid surface, the normal to the wall velocity component was set to zero, whereas the density and pressure were extrapolated from the interior under the assumption that $\partial\rho/\partial n=\partial p/\partial n=0$ or $\partial\rho/\partial y=\partial p/\partial y=0$. It was found that it is required to use high-order-accurate approximations of the derivatives at the wall to retain the accuracy of the numerical solution. For example, the pressure is extrapolated with the following one-seeded, fourth-order-accurate approximation of the first derivative $(\mathrm{d}p/\mathrm{d}y)_1=(-25p_1+48p_2-36p_3+16p_4-3p_5)/12$. The computed results are compared with the exact solution,[22] which gives the time variation of an initial pressure disturbance $p(x,y)=\exp\{-\ell n 2[x^2-(y-y_o)^2]\}$. The initial disturbance is located at $y=y_o$, and, as it spreads, it reflects from a solid wall at $y=0$.

A comparison of the solution computed on an artificially distorted mesh[9] by WENO schemes with $r=3$ and 5 is shown in Fig. 2. Note that the solution computed with the $(r=5)$ ninth-order accurate WENO scheme on the baseline 100×50 point grid, which provides 12 points per wave, is almost indistinguishable from the solution computed with the $(r=3)$ fifth-order-accurate WENO scheme on a 200×100 point grid, refined in both directions. Note that the full WENO scheme with the appropriate smoothness measures must be used for the propagation of the pressure disturbance with the nonlinear Euler equations. Numerical solutions of the liniearized Euler equations that describe the propagation of the acoustic-type pressure disturbance may be possible only with the optimal WENO stencils of Eqs. (12–14).

A grid-independent solution was obtained for the solution computed with the ninth-order-accurate $(r=5)$ WENO scheme because the error does not change for computations performed with the baseline 100×50 point grid and refined 200×100 and 400×200 point grids. Therefore, the errors of the baseline grid are mainly due to the temporal integration scheme. The error of the solutions obtained with different methods, along the normal to the wall symmetry line, is shown in Figs. 3 and 4. Similarly to the WENO scheme that

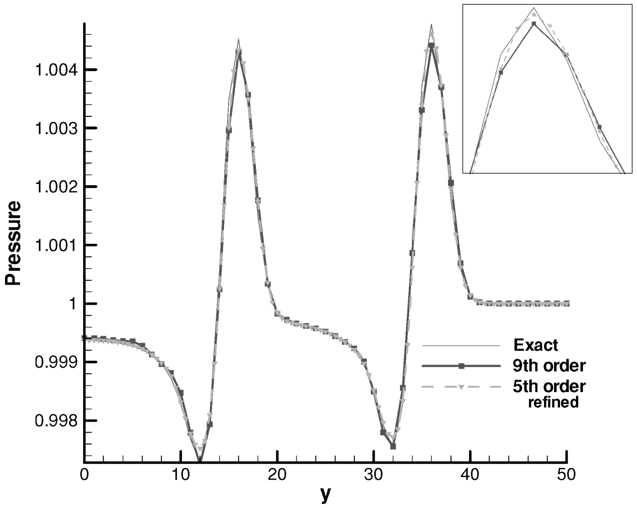

Fig. 2 Comparison of WENO scheme computations with the exact solution.

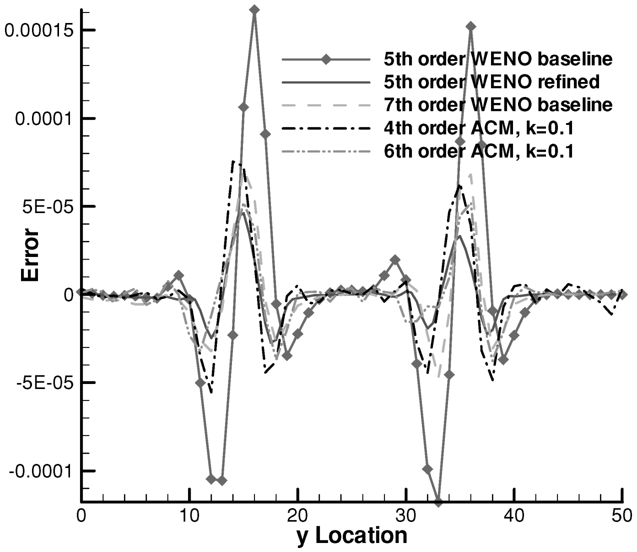

Fig. 3 Comparison of the error obtained with WENO schemes and centered schemes with characteristic-based filters $\kappa=0.1$.

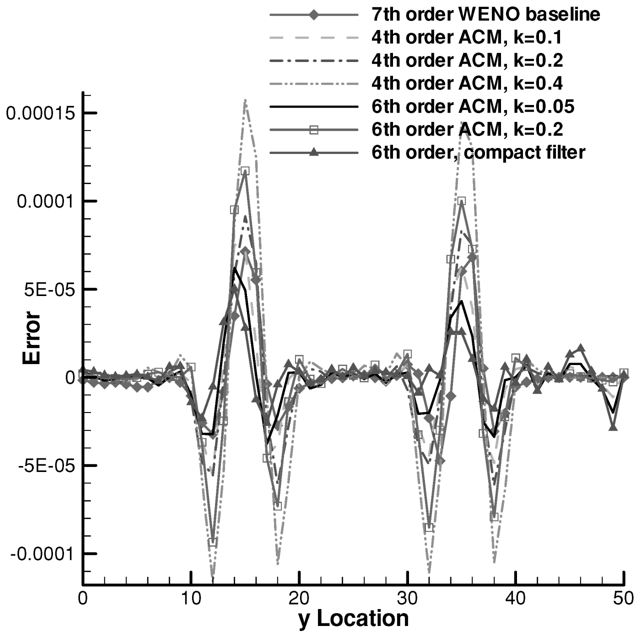

Fig. 4 Effect of the ACM filter parameter on the accuracy of the computed solution.

required use of smoothness, characteristic-based filters are used for the computation of aeroacoustic pulse propagation with the full nonlinear Euler equations. For the comparisons of Fig. 3, the same value of the artificial compression method (ACM) filter parameter ($\kappa = 0.1$) was used. Note that the WENO schemes provide a comparable level of accuracy with the centered schemes.

The effect of the order of the ACM filter parameter on the accuracy of the computed solution is shown in Fig. 4. Note that increase of κ deteriorates the accuracy of the solution. The comparisons of Fig. 4 demonstrate that reduction of the ACM filter parameter κbelow a certain level does not improve the solution. The solution obtained with the spectral-type filter has the smallest error. Among the results compared in Fig. 4, the solution computed with the spectral-type filter was the most efficient. The results computed with the ACM filter required approximately 20% more time compared to the solution obtained with the spectral filter. The solution obtained with the WENO scheme required approximately 30% more time compared to the solution obtained with the spectral filter. Despite the longer computing time, both WENO schemes and the ACM filter provide shock-capturing capability that is of interest in aeronautical applications.

It can be concluded that both the centered and WENO schemes of seventh-order or higher are appropriate for aeroacoustic computations of subsonic flows. For flows with shocks, however, WENO schemes appear to be more appropriate for aeroacoustics because computation of these flows require high values of the ACM filter parameter ($\kappa > 0.5$) to prevent numerical oscillations. Numerical solutions obtained for the same problem on artificially distorted meshes have demonstrated that the accuracy of the solution does not deteriorate when the definition of the metrics is consistent[9,19] and the metrics are computed with a high-order method.

In earlier comparisons, the RK3 of Refs. 6 and 14 was used, even though higher-order or optimized Runge–Kutta methods can further reduce temporal errors. Furthermore, it was found that sufficiently accurate computations of aeroacoustic phenomena can be obtained when implicit time marching is performed with Eq. (2) with $p = 2 - 3$ subiterations within each physical time step. The error of the solutions computed with the explicit RK3 method and the modified implicit BW-24 algorithm[17] with $n = 2$ is almost the same. The error of these computations is shown in Fig. 5.

C. Shock-Capturing Capability

The performance of WENO and centered schemes with characteristic-based filters is evaluated for flows with shocks. The oblique shock reflection problem at $M_\infty = 2.9$ is chosen as the test case. The pressure at $y = 0.5$, computed with WENO schemes of fifth-, seventh-, and ninth-order accuracy is compared with the exact solution in Fig. 6. The computations were performed on a uniformly spaced 200×50 point grid in a domain $-2.0 \leq x \leq 2.0$, $0 \leq y \leq 1.0$. At the left inflow boundary, freestream was specified. At the right outflow boundary, all quantities were extrapolated. On the solid wall at $y = 0$, a slip boundary condition was specified, and at the top, the flow quantities were specified as $\rho = 1.69997$, $u = 2.61934$, $\upsilon = -0.506$, and $p = 1.528$. A sufficient number of ghost points, depending on the order of the scheme, were used at the edges of the domain to retain the formal order of the scheme. For example, computations with the seven-point wide WENO-5 scheme required three ghost points, whereas solutions with the sixth-order accurate ACM method require two ghost points.

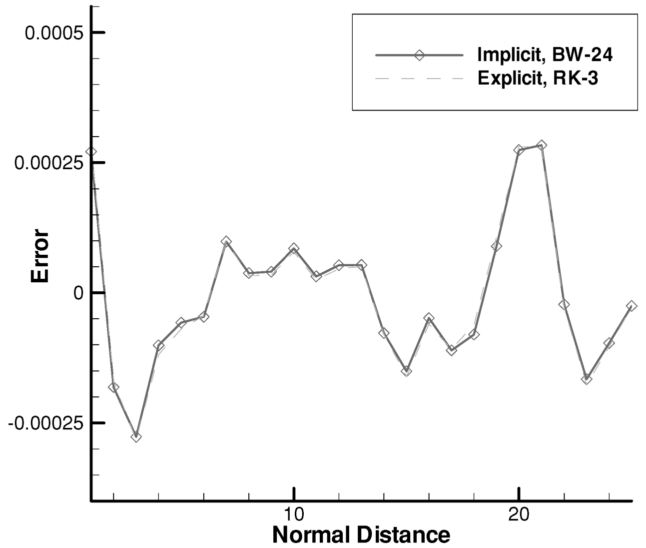

Fig. 5 Error of the solutions computed with implicit and explicit time integration.

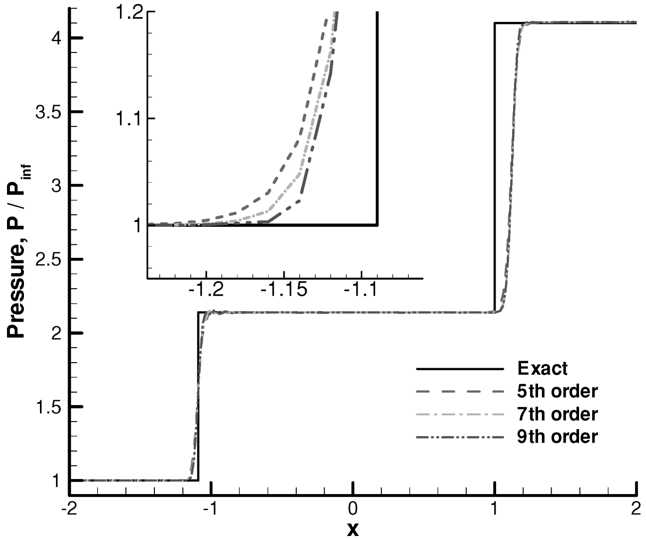

Fig. 6 Comparison of the computed pressure at *y* = 0.5 with the exact solution.

At steady state, an oblique incident shock and a reflected shock were generated. The comparison of the computed pressure with the exact solution of Fig. 6 shows that, as the order of the WENO scheme increases, the computed solution approaches the exact solution. For all computations, the shocks are captured within two cells. The pressure fields obtained from the numerical solutions with the fourth-order-accurate compact centered scheme with $\kappa = 0.7$ and the fifth-order-accurate WENO scheme on an artificially distorted mesh are shown in Fig. 7. Both solutions were computed with the explicit time marching scheme. Note that both methods can capture the oblique strong shock without oscillations. Furthermore, the artificially distorted mesh does not cause oscillations.

The numerical solution for the same problem was computed with the implicit time marching scheme of Eq. (2). The convergence rates of the numerical solutions obtained for different numbers of subiterations are shown in Fig. 8. For reference, the convergence rate of the solution obtained with the explicit Runge–Kutta method[6,14] is also shown in Fig. 8. At convergence, all solutions were the same, and computed pressure and density obtained from implicit or explicit time marching were almost identical.

A comparison of the computed pressure at $y = 0.5$ from the solution obtained with the fifth-order accurate WENO scheme and the solutions obtained with different values of the ACM parameter are shown in Fig. 9. It appears that the computed solution is sensitive to the selection of the ACM parameter. Furthermore, the choice of the upwind TVD limiter[2] affects the solution.

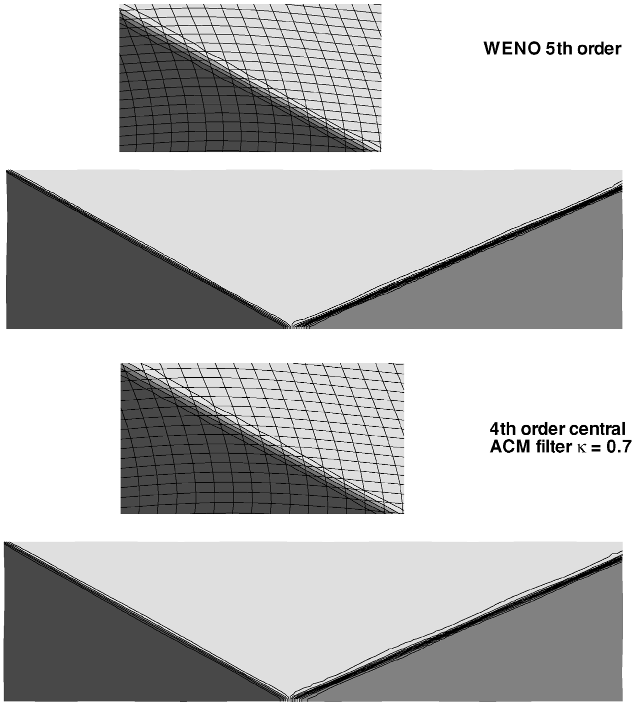

Fig. 7 Pressure fields computed with WENO fifth-order and fourth-order centered scheme with characteristic-based filter (ACM parameter $\kappa = 0.7$) on an artificially distorted mesh.

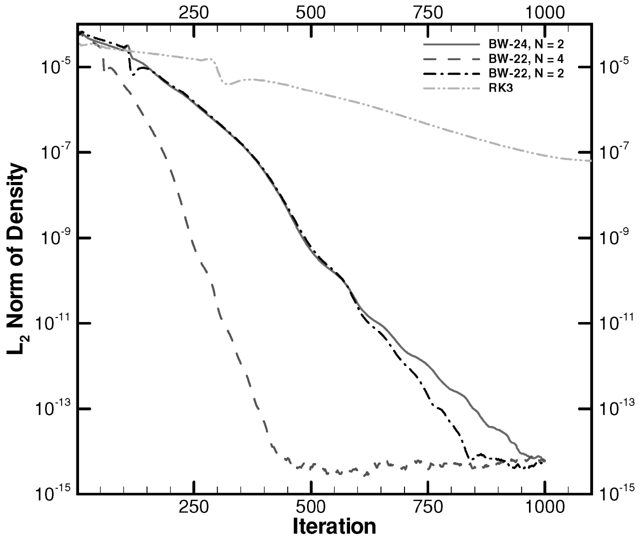

Fig. 8 Convergence rate of solutions computed with implicit time marching.

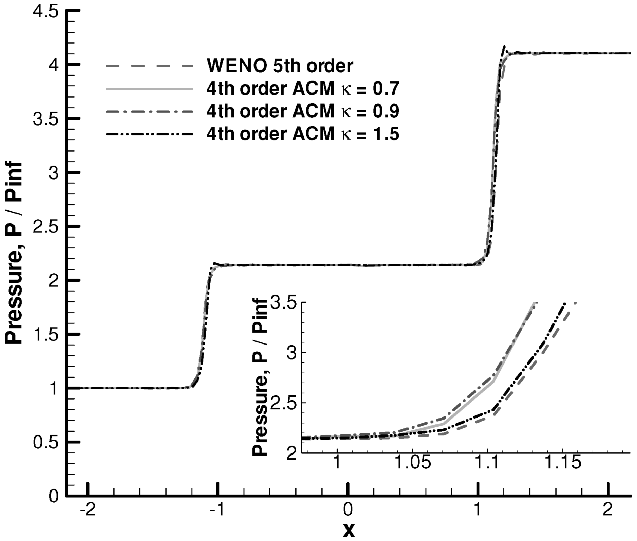

Fig. 9 Effect of ACM parameter on the computed pressure at $y = 0.5$.

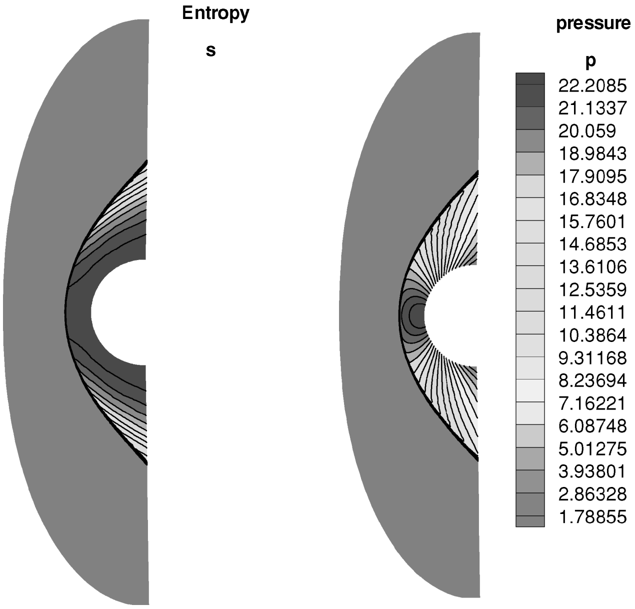

Fig. 10 Computed entropy and pressure fields with the ninth-order-accurate WENO scheme at $M_\infty = 5.0$.

D. Blunt-Body Supersonic Flow

Supersonic flows over a cylinder at various Mach numbers are computed next. These solutions are obtained by the use of WENO schemes. An algebraically generated 181 × 51 point grid was used for this computation of supersonic flows over the cylinder. Similarly to the shock reflection case, a sufficient number of ghost points, depending on the order of the scheme, was used at the edges of the domain. At the inflow, freestream supersonic flow was specified. At the outflow, all quantities were extrapolated from the interior. On the cylinder solid surface, the normal to the surface velocity component was set to zero, and all of the other quantities were extrapolated from the interior with high-order extrapolation and under the assumption that the normal derivative is zero.

The computed pressure and entropy fields at $M_\infty = 5.0$ are shown in Fig. 10. The resolution of the strong shock generated by the high-speed flow is captured without oscillations. Similar to the oblique shock computations of the preceding section, the shock for the supersonic cylinder flow (Fig. 10) is captured within two cells. The

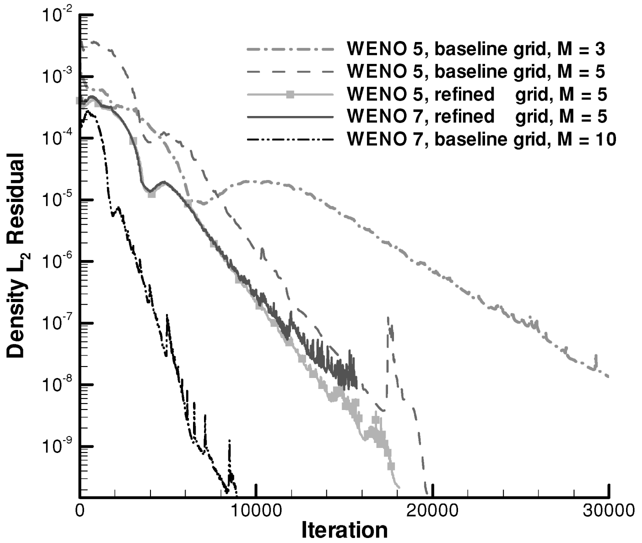

Fig. 11 Convergence history at $M_\infty = 3.0$, 5.0, and 10.0 with the baseline and refined grids.

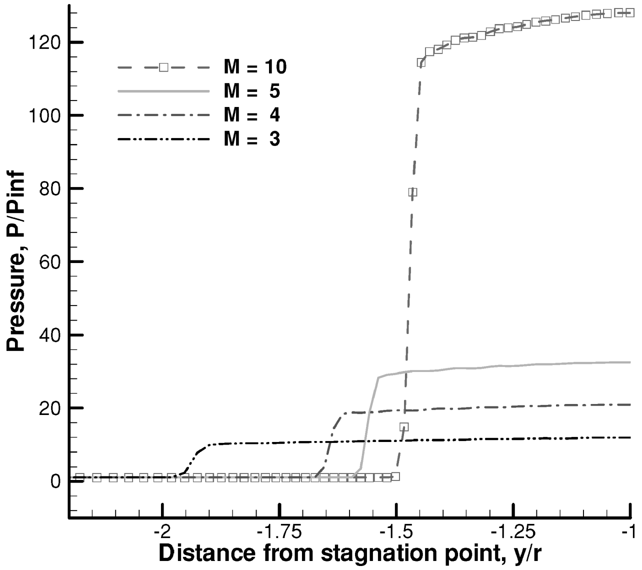

Fig. 12 Pressure at the symmetry line for $M = 3$, 4, 5, and 10.

convergence rates obtained at different Mach numbers, order of accuracy, and for baseline (91 × 51) and refined (181 × 101) grids are shown in Fig. 11. All computations were obtained at the same time step and with the TVD Runge–Kutta method.[6,14] For all cases, the convergence was satisfactory, and the solution practically remained unchanged when the residuals drop four orders of magnitude. A comparison of the computed pressure distributions for the grid line on the symmetry axis that passes through the stagnation point is shown in Fig. 12. Note that the shock is captured within two computational cells and the solution is free from oscillations.

E. Airfoil Flows

Inviscid flows solutions over a NACA-0015 airfoil are computed with the fifth-order-accurate WENO scheme. The computed pressure fields at transonic and supersonic speed are shown in Figs. 13 and 14. The solutions were computed with the explicit time marching scheme on a 261 × 51 point, C-type grid. The airfoil grid included three ghost points at the edges of the domain to use the WENO-5 scheme for the entire domain without dropping the stencil accuracy at the airfoil surface and the wake. The supersonic and transonic flow computations were obtained on the same grid. For both flow speeds, a smooth solution is obtained on the highly stretched, high-aspect-ratio, C-type grid.

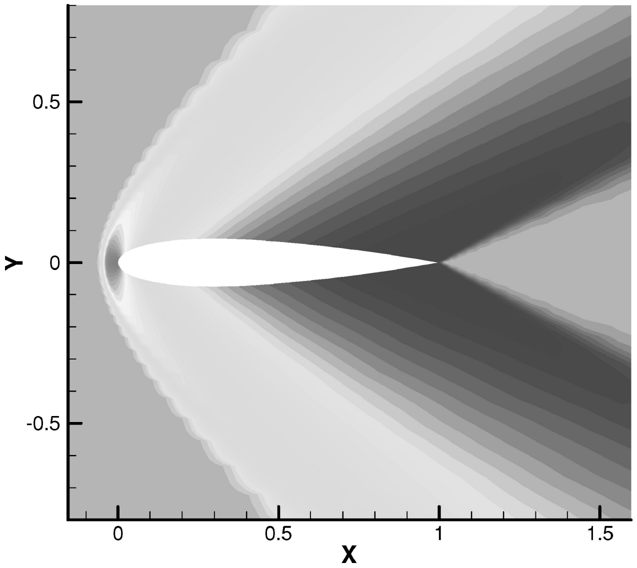

Fig. 13 Computed pressure field over a NACA-0015 airfoil for supersonic flow; $M = 2.0$ and $\alpha = 0.0$ deg.

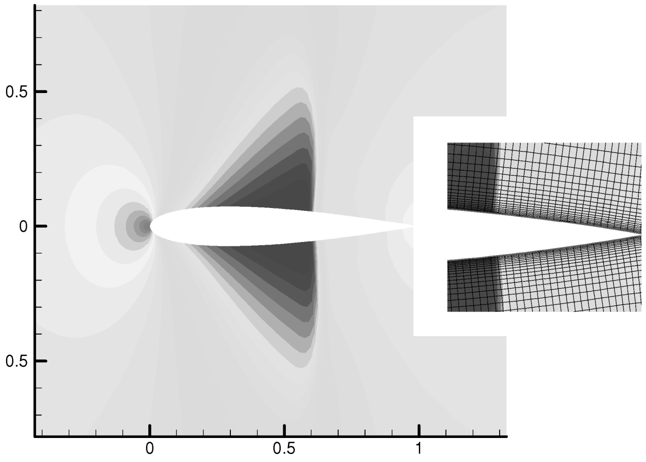

Fig. 14 Computed pressure field over a NACA-0015 airfoil for transonic flow; $M = 0.8$ and $\alpha = 0.1$ deg.

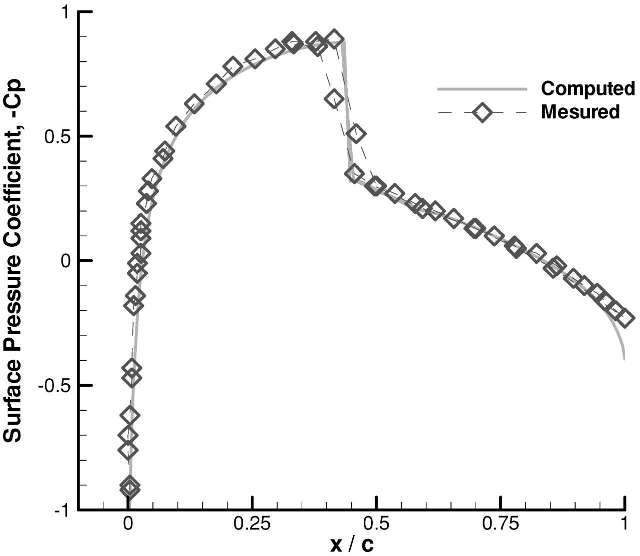

Fig. 15 Comparison of the computed pressure surface pressure coefficient for NACA-0012 airfoil at $M = 0.8$ and $\alpha = 0.1$ deg with the experiment.

The computed pressure field at $M_\infty = 2.0$ is shown in Fig. 13. The computed pressure field shows adequate resolution of the leading-edge bow shock and the two shocks at the trailing edge, despite the coarseness of the grid. The same type of inflow/outflow and solid wall boundary conditions as the supersonic cylinder flow were used. At the wake of the C-type grid, averaging was used.

For the transonic flow computation at $M_\infty = 0.8$, the shocks of the upper and lower surface shown by the pressure contours of Fig. 14 are well resolved. For this computation, the inflow and outflow boundary conditions were specified with one-dimensional Riemann invariants. A comparison of the computed surface pressure coefficient for transonic flow over the NACA-0012 airfoil with the experimental data is shown in Fig. 15. The overall agreement of the computed inviscid solution with the experiment is satisfactory, and the shock is resolved within two cells.

V. Conclusions

High-order-accurate finite difference schemes for the compressible flow equations have been evaluated for test problems. The ability of high-order discretizations to perform long time convection carries over to the propagation of aeroacoustic disturbances with the full Euler equations. For aeroacoustics of complex flows with discontinuities, high-order WENO schemes have an advantage because they provide the required accuracy level, and they do not require adjustment of parameters. WENO schemes were found accurate and robust for the computation of supersonic and transonic flows in general geometries. For these flows, the centered schemes with characteristic-based filters require careful selection of the ACM parameter. These methods are, however, more efficient, and they can be used once the ACM parameter is chosen according to the flow features, as suggested in Ref. 1.

Acknowledgments

The author gratefully acknowledges the NAS2-01016, Phase II SBIR contract, monitored by William Warmbrodt and Roger Strawn, which supported part of this work.

References

[1] Garnier, E., Mossi, M., Sagaut, P., Comte, P., and Deville, M., “On the Use of Shock-Capturing Schemes for Large-Eddy Simulations,” *Journal of Computational Physics*, Vol. 153, No. 2, 1999, pp. 273–311.

[2] Yee, H. C., Sandham, N. D., and Djomehri, M. J., “Low-Dissipative High-Order Shock-Capturing Methods Using Characteristic-Based Filters,” *Journal of Computational Physics*, Vol. 150, No. 2, 1999, pp. 199–238

[3] Gaitonde, D. V., and Visbal, M. R., “Pade-Type High-Order Boundary Filters for the Navier–Stokes Equations,” *AIAA Journal*, Vol. 38, No. 11, 2000, pp. 2103–2112.

[4] Lele, S. K., “Compact Finite Difference Schemes with Spectral-Like Resolution,” *Journal of Computational Physics*, Vol. 103, No. 1, 1992, pp. 16–42.

[5] Harten, A., Engquist, B., Osher, S., and Chakravarthy, S., “Uniformly High-Order Essentially Non Oscillatory Schemes, III,” *Journal of Computational Physics*, Vol. 71, No. 2, 1987, pp. 213–303.

[6] Shu, C.-W., and Osher, S., “Efficient Implementation of Essentially Non-Oscillatory Shock-Capturing Schemes,” *Journal of Computational Physics*, Vol. 77, No. 1, 1988, pp. 439–471.

[7] Jiang, G. S., and Shu, C.-W., “Efficient Implementation of Weighted ENO Schemes,” *Journal of Computational Physics*, Vol. 126, No. 1, 1996, pp. 202–244.

[8] Visbal, M. R., and Gaitonde, D. V., “High-Order Accurate Methods for Complex Unsteady Subsonic Flows,” *AIAA Journal*, Vol. 37, No. 10, 1999, pp. 1231–1239.

[9] Visbal, M. R., and Gaitonde, D. V., “On the Use of High-Order Finite-Difference Schemes on Curvilinear and Deforming Meshes,” *Journal of Computational Physics*, Vol. 181, No. 1, 2002, pp. 155–185.

[10] Rizzetta, D. P., Visbal, M. R., and Gaitonde, D. P., “Large-Eddy Simulation of Supersonic Compression Ramp Flow by High-Order Method,” *AIAA Journal*, Vol. 39, No. 12, 2001, pp. 2283–2292.

[11] Harten, A., “The Artificial Compression Method for Computation of Shock and Contact Discontinuities: III Self Adjusting Hybrid Schemes,” *Mathematics of Computation*, Vol. 32, 1978, pp. 363–393.

[12] Gustafsson, B., and Olsson, P., “Fourth–Order Difference Methods for Hyperbolic IBVPs,” *Journal of Computational Physics*, Vol. 117, No. 2, 1995, pp. 300–317.

[13] Pirozzoli, S., “Conservative Hybrid Compact-WENO Schemes for Shock-Turbulence Interaction,” *Journal of Computational Physics*, Vol. 178, No. 1, 2002, pp. 81–117.

[14] Cocburn, B., and Shu, C.-W., “The Runge–Kutta Discontinuous Galerkin Method for Conservation Laws,” *Journal of Computational Physics*, Vol. 141, No. 2, 1998, pp. 199–224.

[15] Gottlieb, S., and Shu, C.-W., “Total Variation Diminishing Runge–Kutta Schemes,” *Mathematics of Computation*, Vol. 67, 1998, pp. 73–85.

[16] Beam, R., and Warming, R., “Implicit Finite-Difference Algorithms for Hyperbolic Systems in Conservation-Law Form,” *Journal of Computational Physics*, Vol. 22, No. 1, 1976, pp. 87–110.

[17] Ekaterinaris, J. A., “Implicit, High-Resolution, Compact Schemes for Gas Dynamics and Aeroacoustics,” *Journal Of Computational Physics*, Vol. 156, No. 1, 1999, pp. 272–299.

[18] Carpenter, M. H., Gottlieb, D., and Abarbanel, S., “The Stability of Numerical Boundary Treatments for Compact High-Order Finite-Difference Schemes,” *Journal of Computational Physics*, Vol. 108, No. 2, 1993, pp. 272–295.

[19] Vinokur, M., and Yee, H. C., “Extension of Efficient Low Dissipation High Order Schemes for 3-D Curvilinear Moving Grids,” NASA TM 209598, June 2000.

[20] Shu, C.-W., “High Order ENO and WENO Schemes for Computational Fluid Dynamics,” *High-Order Methods for Computational Physics*, edited by T. J. Barth and H. Deconinck, Springer-Verlag, Berlin, 1999, pp. 439–582.

[21] Balsara, D. S., and Shu, C.-W., “Monotonicity Preserving Weighted Essentially Non-Oscillatory Schemes with Increasingly High Order of Accuracy,” *Journal of Computational Physics*, Vol. 160, No. 2, 2000, pp. 405–452.

[22] Hardin, J. D., Ristorcelli, J. R., and Tam, C. K., *ICASE/LaRC Workshop on Benchmark Problems in Computational Aeroacoustics (CAA)*, NASA CP 3300, 1995.

S. Mahalingam
Associate Editor